

**The Role of Impurities in the Kinetic Persistence of Amorphous Calcium Carbonate: A Nanoscopic Dynamics View**

Ayumi Koishi,<sup>1</sup> Alejandro Fernandez-Martinez,<sup>\*1</sup> Beatrice Ruta,<sup>2,3</sup> Monica Jimenez-Ruiz,<sup>4</sup> Roberta Poloni,<sup>5</sup> Devis di Tommaso,<sup>6</sup> Federico Zontone,<sup>3</sup> Glenn A. Waychunas,<sup>7</sup> German Montes-Hernandez<sup>1</sup>

<sup>1</sup>Univ. Grenoble Alpes, Univ. Savoie Mont Blanc, CNRS, IRD, IFSTTAR, ISTERre, Grenoble, France

<sup>2</sup>Univ. Lyon, Université Claude Bernard Lyon 1, CNRS, Institut Lumière Matière, Villeurbanne, France

<sup>3</sup>ESRF – The European Synchrotron, Grenoble, France

<sup>4</sup>Institut Laue Langevin, Grenoble, France

<sup>5</sup>SIMAP, CNRS and Univ. Grenoble Alpes, Grenoble, France

<sup>6</sup>Queen Mary University of London, London, United Kingdom

<sup>7</sup>Earth and Environmental Sciences Area, Lawrence Berkeley National Laboratory, Berkeley, United States

[\\*Alex.Fernandez-Martinez@univ-grenoble-alpes.fr](mailto:Alex.Fernandez-Martinez@univ-grenoble-alpes.fr)

Phone: +33 476635197

## Table of contents

<b>1. Supporting Figures and Tables</b> .....	S3
<b>Supporting Table S1.</b> Solution chemistry of syntheses and resulting sample compositions.....	S3
<b>Supporting Table S2.</b> Coherent and incoherent cross-section values for selected elements and isotopes ...	S3
<b>Supporting Figure S1.</b> ATR-FTIR spectra collected for the verification of the synthesized solid samples.	S4
<b>Supporting Figure S2.</b> Representative 2D speckle patterns and schematic illustration of XPCS data analysis.....	S5
<b>Supporting Figure S3.</b> Representative thermogravimetry and calorimetry curves .....	S6
<b>Supporting Figure S4.</b> Comparison of experimental GDOS (experimental) and DFT-calculated VDOS for water and monohydrocalcite .....	S7
<b>Supporting Figure S5.</b> Ab initio VDOS of water in the first hydration shell of aqueous $\text{Ca}^{2+}$ and $\text{Mg}^{2+}$ ....	S8
<b>Supporting Figure S6.</b> Librational region of the GDOS for $\text{Sr}^{2+}$ - and $\text{Ba}^{2+}$ -doped ACC.....	S9
<b>Supporting Figure S7.</b> ATR-FTIR spectra tracked over the duration of 1.5 month.....	S10
<b>Supporting Figure S8.</b> Aging dynamics.....	S11
<b>Supporting Figure S9.</b> Verification of X-ray damage and X-ray induced aging .....	S12
<b>Supporting Figure S10.</b> Reproduction of dehydration conditions .....	S13
<b>Supporting Figure S11.</b> Relaxation time $\tau$ as a function of scattering vector $q$ .....	S14
<b>2. Computational Simulations Methods</b> .....	S15
<b>3. Classical nucleation theory: linking solid state dynamics and crystallization kinetics</b> .....	S17

## 1. Supporting Figures and Tables

**Supporting Table S1.** Solution chemistry of syntheses and resulting sample compositions

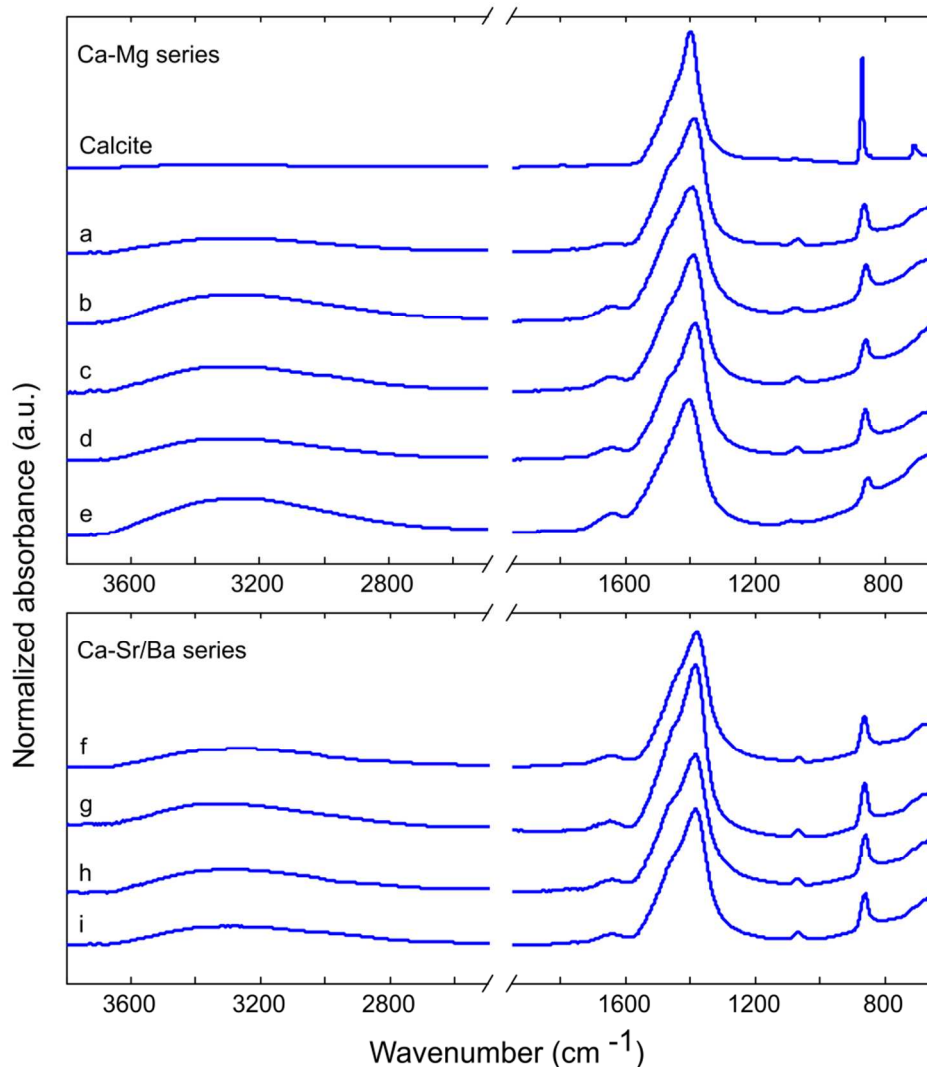
$\text{Ca}_{1-x}\text{Mg}_x\text{CO}_3 \cdot n\text{H}_2\text{O}$				$\text{Ca}_{1-x}\text{M}_x\text{CO}_3 \cdot n\text{H}_2\text{O}$ (M = $\text{Sr}^{2+}$ or $\text{Ba}^{2+}$ )			
$x$	$\text{Ca}^{2+}$ [M]	$\text{Mg}^{2+}$ [M]	$\text{CO}_3$ [M]	$x$	$\text{Ca}^{2+}$ [M]	$\text{M}^{2+}$ [M]	$\text{CO}_3$ [M]
0	0.02	0	0.02 (+ 2M NaOH)	-	-	-	-
0.08	0.045	0.015	0.06	0.3	0.045	0.015	0.06
0.35	0.03	0.03	0.06	0.5	0.03	0.03	0.06
0.7	0.015	0.045	0.06	-	-	-	-
1	0	0.1	0.1	-	-	-	-

$x$  values report the measured values of the synthesized samples.  $\text{Sr}^{2+}$  and  $\text{Ba}^{2+}$  series were synthesized for comparison purpose, therefore were prepared with only two conditions.

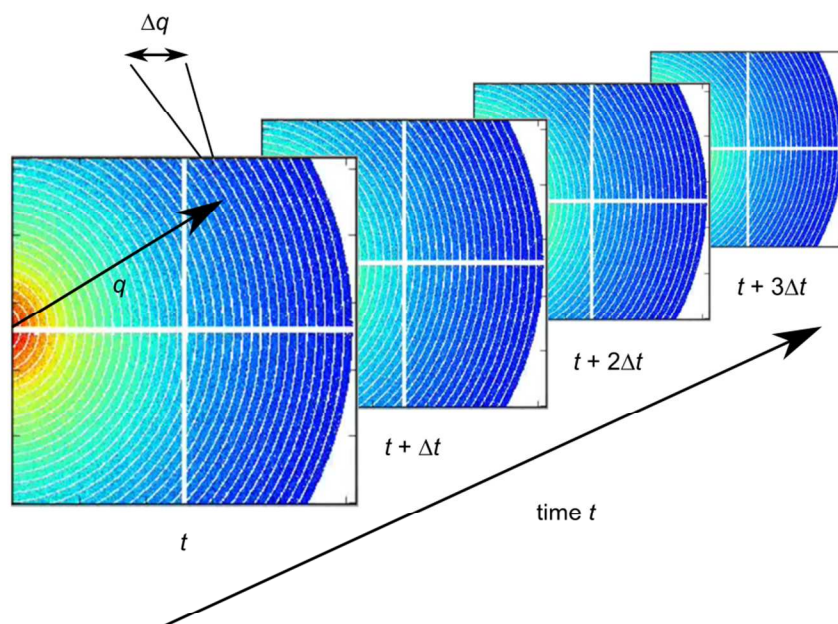
**Supporting Table S2.** Coherent and incoherent cross-section values for selected elements and isotopes

Element	Thermal neutrons	
	$\sigma_{\text{coh}}$ (barn)	$\sigma_{\text{inc}}$ (barn)
$^1\text{H}$	1.76	80.3
$^2\text{H}$	5.59	2.05
$^{\text{nat}}\text{C}$	5.55	0.001
$^{\text{nat}}\text{Ca}$	2.78	0.05
$^{\text{nat}}\text{O}$	4.23	0.0008

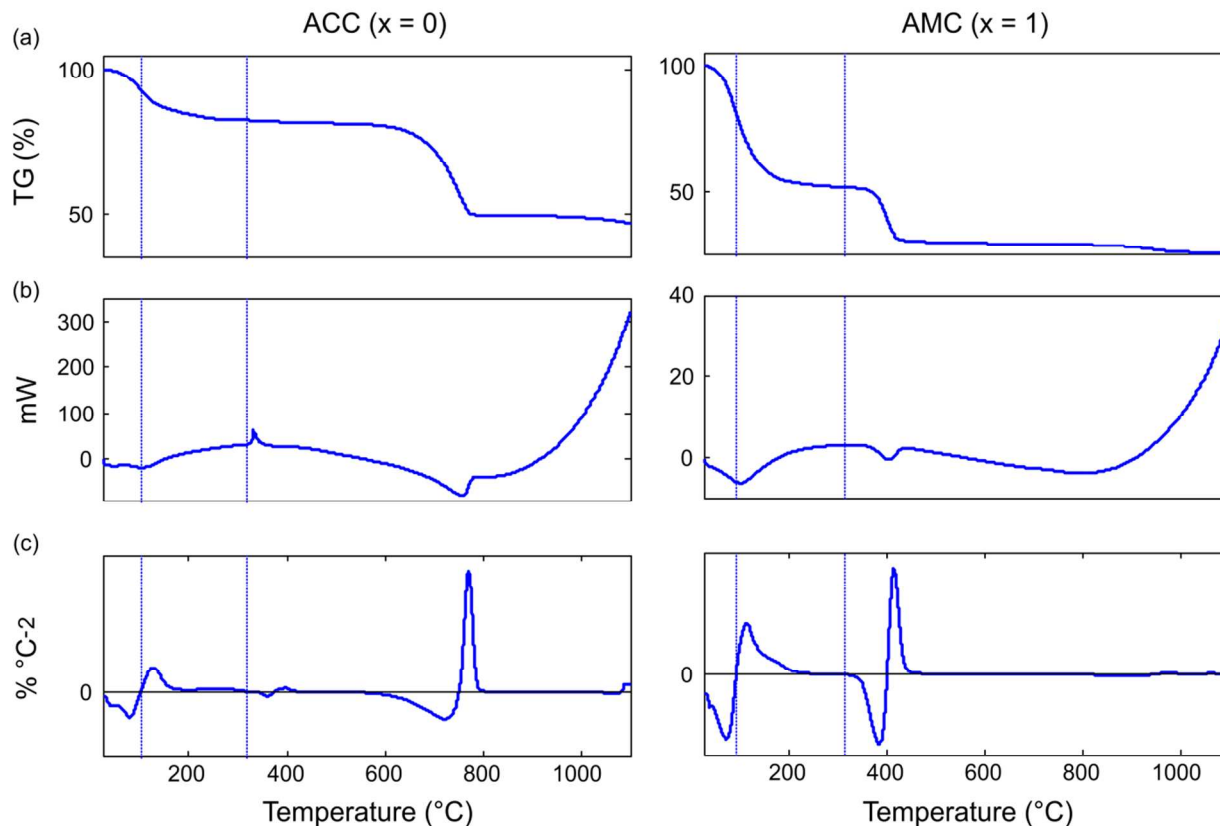
$\sigma = 4\pi|b|^2$  where  $b$  is the scattering length<sup>1</sup>.



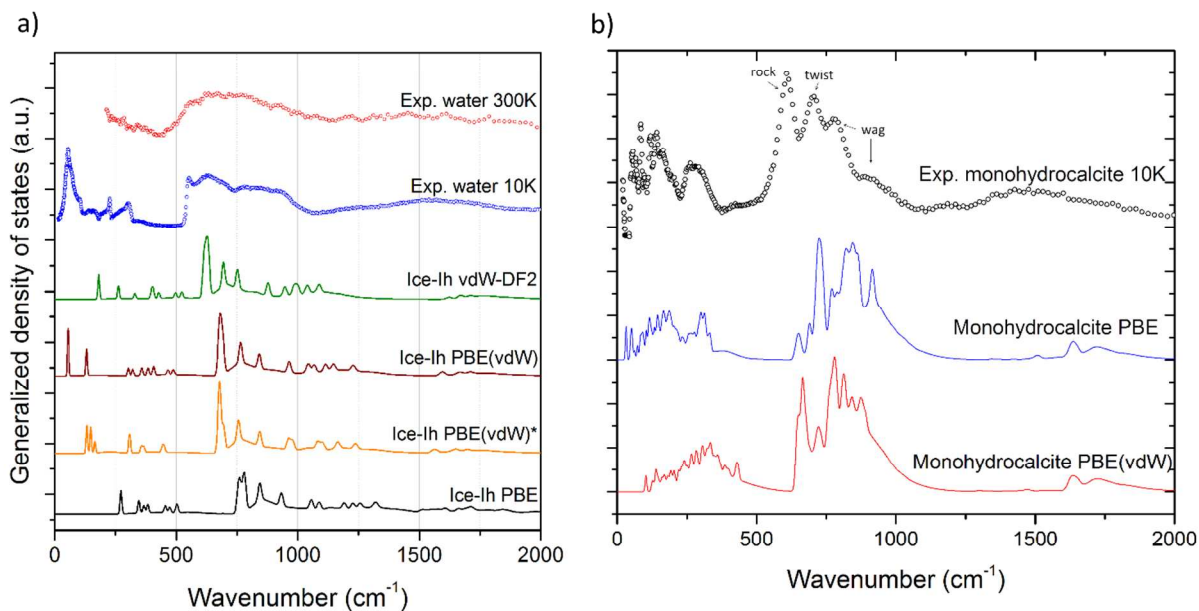
**Supporting Figure S1.** ATR-FTIR spectra collected for the verification of the synthesized solid samples. Spectra are normalized to the maximum intensity of the carbonate species ( $\approx 1400\text{ cm}^{-1}$ ). Top:  $\text{Mg}^{2+}$ -doped series, with calcite spectra as reference, for (a)  $x = 0$ , pure ACC, (b)  $x = 0.08$ , (c)  $x = 0.35$ , (d)  $x = 0.7$ , and (e)  $x = 1$ . Bottom: (f)  $x = 0.25$  and (g)  $x = 0.49$  for  $\text{Sr}^{2+}$ -doped series and (h)  $x = 0.29$  and (i)  $x = 0.52$  for  $\text{Ba}^{2+}$ -doped series. Notice the following characteristics absent in calcite reference spectra: the presence of adsorbed water (broad band between  $3600$  and  $2800\text{ cm}^{-1}$ ), structural water (small peak at  $\sim 1620\text{ cm}^{-1}$ ), doublet band corresponding to  $\text{CO}_3^{2-}$  asymmetric stretch around  $1400\text{ cm}^{-1}$ , characteristic to amorphous carbonates, as well as the position of the peak corresponding to  $\text{CO}_3^{2-}$  bending ( $\approx 860\text{ cm}^{-1}$ ), shifted from that of calcite ( $\approx 871\text{ cm}^{-1}$ ).



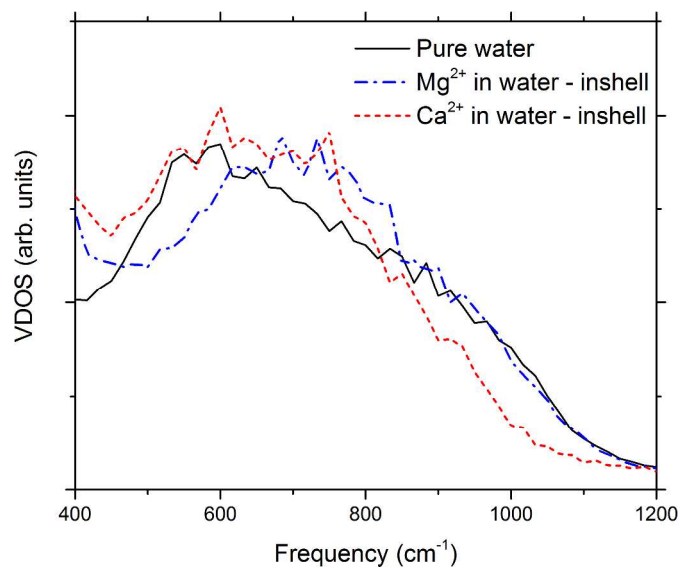
**Supporting Figure S2.** Representative 2D speckle patterns and schematic illustration of XPCS data analysis. The intensity autocorrelation functions (see main text) were computed from an ensemble of these time-resolved images at a given  $q$  with a certain width.



**Supporting Figure S3.** Representative thermogravimetry and calorimetry curves for ACC (left) and AMC (right). The determination of mobile and rigid water regimes were determined based on the first two inflection points found on the second derivative curves of TGA (c), indicated by dotted guidelines. The DSC curve of ACC generally exhibits two endothermic peaks: a first broad peak at around 100°C, indicative of a dehydration of adsorbed water, and a second at around 750°C, indicative of decarbonation from calcite to CaO. The sharp exothermic peak, observed at around 320 °C, indicates crystallization of ACC into calcite. For Mg<sup>2+</sup>-doped ACCs, absence of sharp crystallization peaks and the presence of two endothermic peaks (one at ~100 °C for dehydration and the other at ~400 °C for decarbonation) were the common features of DSC curves.

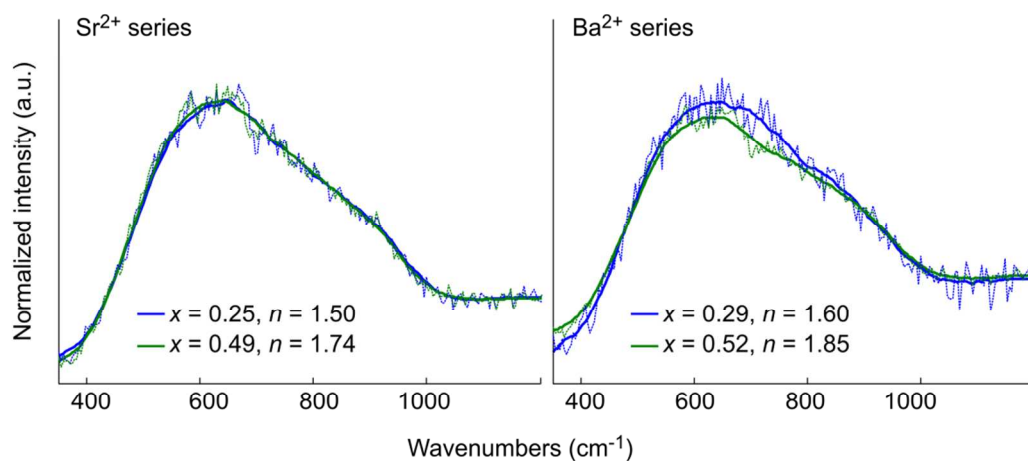


**Supporting Figure S4.** Comparison of experimental GDOS and DFT-calculated VDOS for water and monohydrocalcite. (a) Water at 300K and at 10K (hexagonal ice) and a benchmark study of different DFT functionals to reproduce the hexagonal ice VDOS. \*No partial core corrections were applied for the generation of the oxygen pseudopotential. (b) Experimental GDOS and computational VDOS of monohydrocalcite. The structural water in monohydrocalcite shows well-defined librational spectra, showing three distinct peaks in the  $\sim 500 - 1000 \text{ cm}^{-1}$  region. These DFT calculations have allowed assigning these peaks to the rock, wagging and twisting water librational modes.

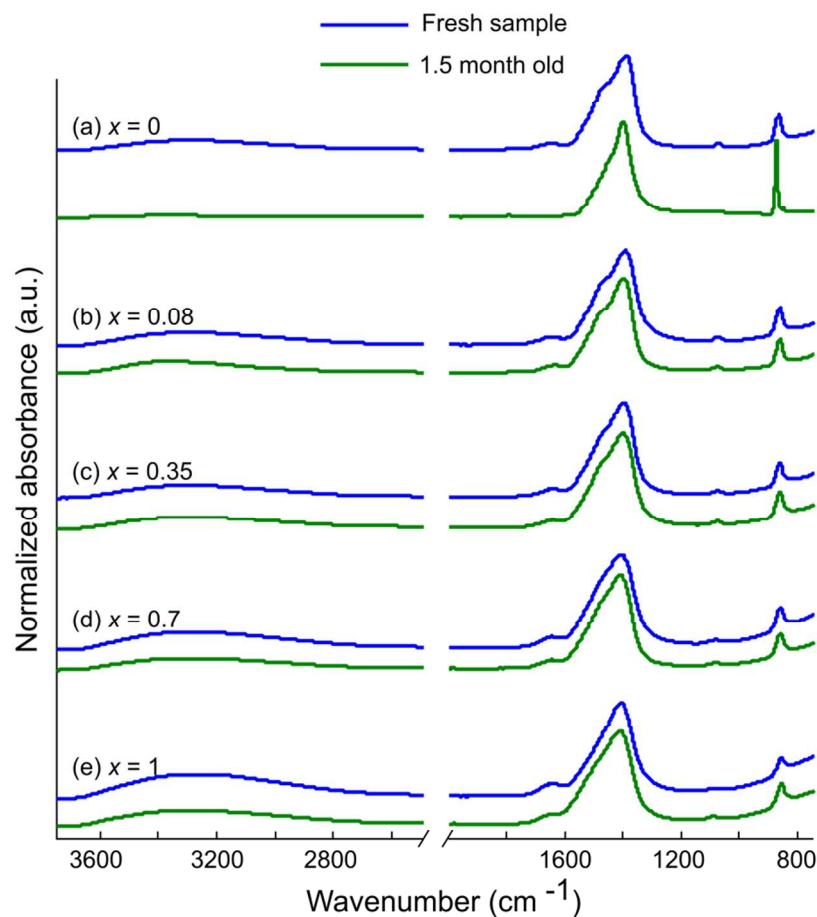


**Supporting Figure S5.** Ab initio VDOS of water in the first hydration shell of aqueous  $\text{Ca}^{2+}$  and  $\text{Mg}^{2+}$  and pure water (300K). A shift towards higher energies can be observed for the  $\text{Mg}^{2+}$  in comparison to the  $\text{Ca}^{2+}$  hydration water. The spectra indicate the same trend observed for  $\text{Mg}^{2+}$ -doped ACC at 10 K (see main text), pointing to a stiffening of H-bonding.

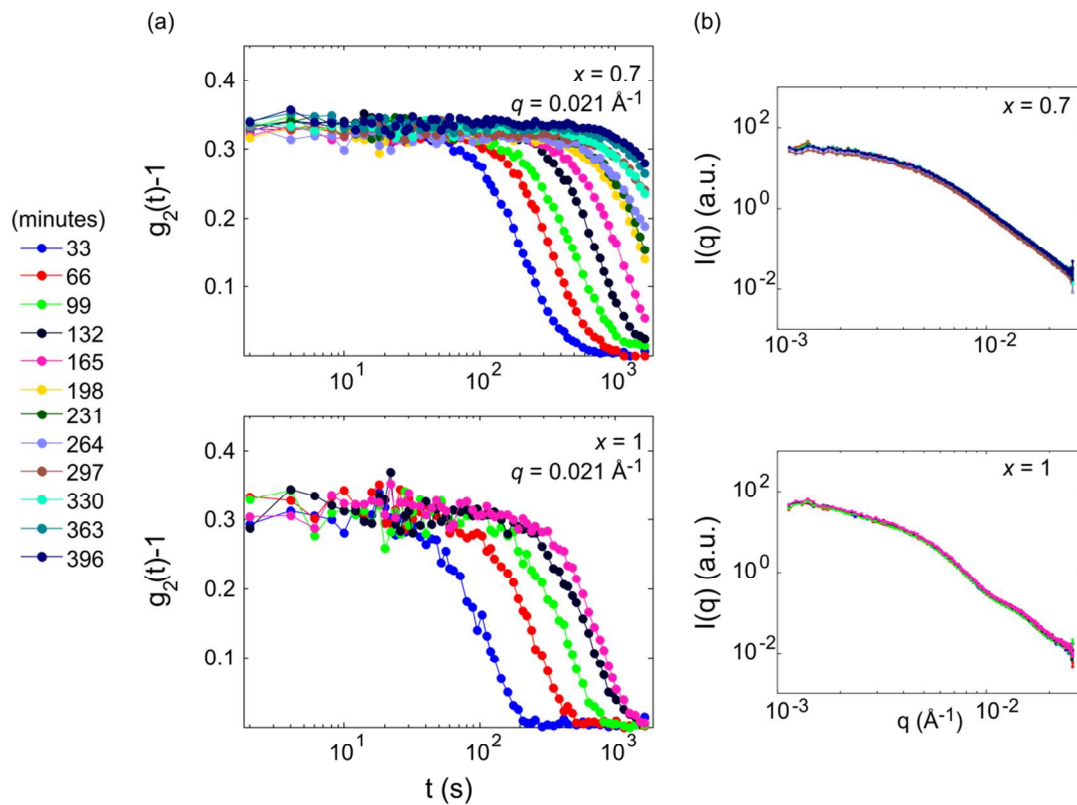




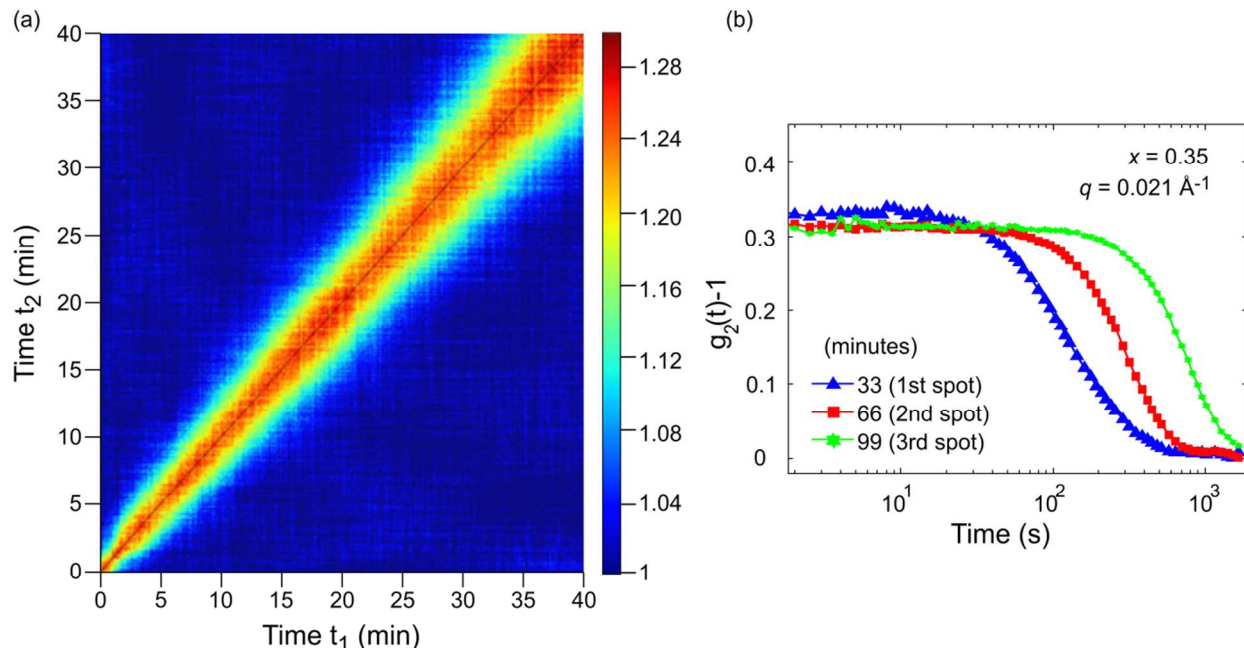
**Supporting Figure S6.** Librational region of the GDOS for  $\text{Sr}^{2+}$ - and  $\text{Ba}^{2+}$ -doped ACC. Varying  $\text{Sr}^{2+}/\text{Ca}^{2+}$  or  $\text{Ba}^{2+}/\text{Ca}^{2+}$  ratio resulted in no change of intensity above  $850\text{ cm}^{-1}$ , indicating that there is no stiffening of H-bonding network when  $\text{Sr}^{2+}$  or  $\text{Ba}^{2+}$  is incorporated. Note that the  $n$  values reported here are from the corresponding samples immediately after the synthesis and not at the corresponding time of the actual IINS measurements, as is done for  $\text{Mg}^{2+}$ -doped ACC, thus may be overestimated.



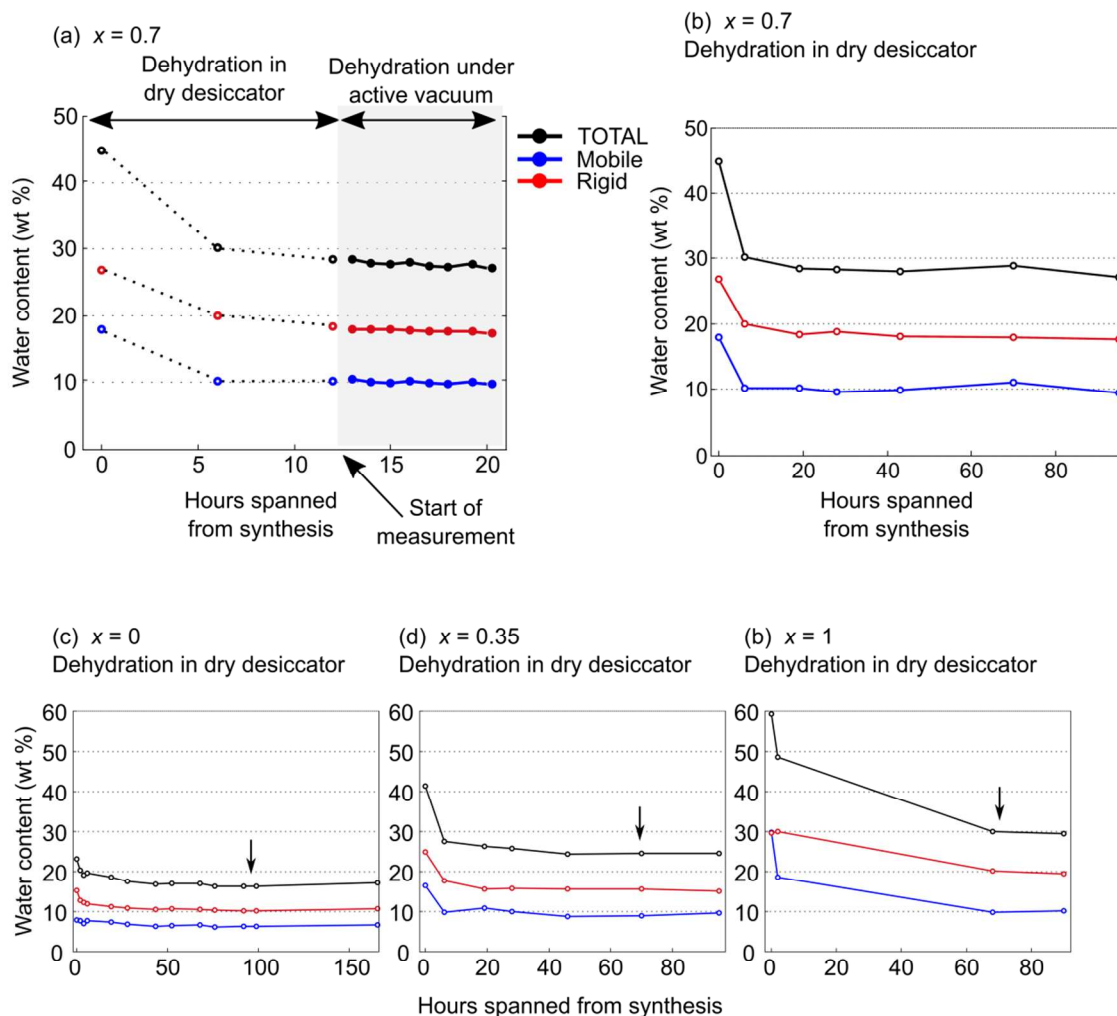
**Supporting Figure S7.** ATR-FTIR spectra tracked over the duration of 1.5 month for (a)  $x = 0$ , pure ACC, (b)  $x = 0.08$ , (c)  $x = 0.35$ , (d)  $x = 0.7$ , and (e)  $x = 1$ . Notice the persistent presence of both adsorbed (broad band between 3600 and 2800 cm<sup>-1</sup>) and structural (small peak at ~1620 cm<sup>-1</sup>) water for samples  $x \geq 0.08$  after 1.5 month, while the pure ACC ( $x = 0$ ) has transformed into calcite with its characteristic peak at 871 cm<sup>-1</sup>. Note also that occasionally, syntheses of pure ACC resulted in an immediate crystallization of calcite, while this, in our experimental conditions employed, was never observed when Mg<sup>2+</sup> was present even at a very low content (results not shown).



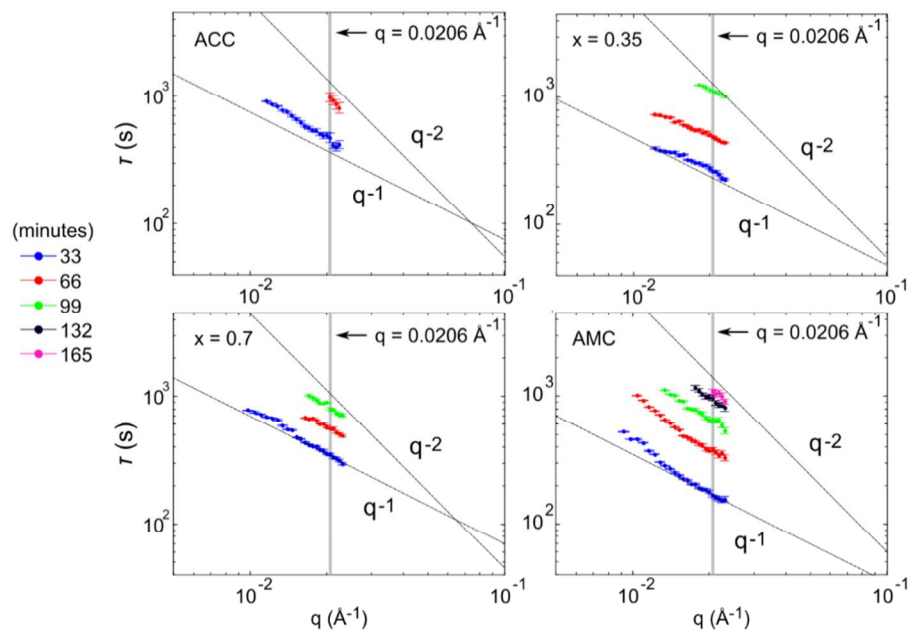
**Supporting Figure S8.** Aging dynamics. (a) Time-evolution of intensity autocorrelation functions for  $\text{Ca}_{(1-x)}\text{Mg}_x\text{CO}_3 \cdot n\text{H}_2\text{O}$ , with  $x = 0.7$  and  $1$  (AMC) at  $q = 0.021 \text{ \AA}^{-1}$  ( $d \sim 30.6 \text{ nm}$ ), obtained for every 1000 images, corresponding to an experimental time of 33 min. (b) Evolution of the static intensity profile,  $I(q)$ , for the full  $q$  range measured ( $0.001 \leq q \leq 0.022$ ).



**Supporting Figure S9.** Verification of X-ray damage and X-ray induced aging. (a) Representative two-time correlation function calculated at  $q = 0.021 \text{ \AA}^{-1}$  ( $d \approx 30.6 \text{ nm}$ ) for sample  $x = 1$  (AMC), showing continuous aging over the course of the measurement. (b) Intensity auto-correlation functions for  $\text{Ca}_{0.65}\text{Mg}_{0.35}\text{CO}_3 \cdot 1.70\text{H}_2\text{O}$ , measured at three different spots with a minimum spacing of  $100 \mu\text{m}$  between them (on the same sample), to test a possibility of X-ray induced reverse stimulation of the dynamics without any apparent damage. The intensity auto-correlations at the three spots exhibited a slowing down accordingly to the order of irradiated spots (spot 1  $\rightarrow$  2  $\rightarrow$  3). This confirms that the aging is independent on the accumulated dose of radiation at a given sample position but it occurs in the whole sample. From these observations, beam-induced aging can be safely excluded as being responsible for the aging dynamics.



**Supporting Figure S10.** Reproduction of dehydration conditions. (a) Time-evolution of dehydration and water distribution between mobile and rigid regimes determined from TGA curves for  $\text{Ca}_{0.3}\text{Mg}_{0.7}\text{CO}_3 \cdot n\text{H}_2\text{O}$  ( $4.02 \geq n \geq 1.84$ ) in a reproduced condition as the corresponding sample underwent before and during XPCS measurement and (b) in a dry desiccator. The XPCS data for the corresponding sample was collected after  $\sim 12$  hours from the synthesis. The  $x$ -axis shows the time spanned from the synthesis of the sample (stored in the desiccator) to the XPCS measurements (light grey region). (c, d, e) Time-evolution of dehydration and water distribution between the mobile and rigid regimes in a dry desiccator for  $\text{Ca}_{1-x}\text{Mg}_x\text{CO}_3 \cdot n\text{H}_2\text{O}$  with (c)  $x = 0$  ( $1.67 \geq n \geq 1.08$ ), (d)  $x = 0.35$  ( $3.70 \geq n \geq 1.71$ ), (e)  $x = 0.7$  ( $6.80 \geq n \geq 1.94$ ), determined by TGA. Arrows indicate the approximate time at which XPCS measurement was begun for the corresponding sample. Along the TGA measurement, the amorphous state of all the samples at all the times shown here was verified by ATF-FTIR. Note that most of the dehydration takes place during the first  $\sim 10$  hours. Active vacuum resulted in only a slight dehydration (maximum change of 2% w/w). For samples  $x = 0, 0.35$  and  $1$ , only the water loss in a dry desiccator is reported since the loss of water under active vacuum can be negligible, although this small dehydration under active vacuum could be responsible for the observed aging behavior (see main text).



**Supporting Figure S11.** Relaxation time  $\tau$  as a function of scattering vector  $q$ , and its evolution with the experimental time (in different colors) for samples  $x = 0$  (ACC),  $x = 0.35$ ,  $x = 0.7$  and  $x = 1$  (AMC). The lines indicate the theoretical  $q$ -dependence for a purely Brownian diffusion ( $q^{-2}$ ) and for ballistic dynamics ( $q^{-1}$ ). See Supporting Information section 3. Classical nucleation theory for detailed information.

## 2. Computational Simulations Methods

### 2.1. Density Functional Theory calculations of the vibrational density of states: ice and monohydrocalcite

DFT calculations of the vibrational densities of state of ice and monohydrocalcite were performed using the SIESTA package.<sup>2</sup> Norm-conserving Trouiller-Martins pseudopotentials are used in all calculations.<sup>3</sup>  $2s$  and  $2p$  electrons of C and O atoms are explicitly included in the valence; for all the Mg and Ca semicore electrons are considered, specifically,  $2s$ ,  $2p$  and  $3s$  for Mg,  $3s$ ,  $3p$  and  $4s$  for Ca. We use a variationally-optimized cite double-zeta polarized basis including d-orbitals for C, and O atoms.<sup>4,5</sup> The integration over the irreducible Brillouin zone is carried using a  $3 \times 3 \times 5$  Monkhorst-Pack grid. Real space integrals are performed on a mesh with a 300 Ry cutoff. For each calculation, we optimize the atomic positions until the forces are smaller than 20 meV/Å. The Hellmann–Feynman forces were calculated for all the atoms in the system, fully building the dynamical matrix using a finite difference approach. We computed the lattice dynamics for a primitive cell of hexagonal ice water, monohydrocalcite (72 atoms) and a Mg-replaced unit cell where we only replace one Ca atom out of the six. We employed the vdW-DF2 functional,<sup>6</sup> the same functional in which we replace the PW86R parametrization for the exchange by PBE, and the PBE functional<sup>7</sup> in order to benchmark the librational modes of ice water against experiments. The neutron scattering length weighted VDOS were calculated from the dynamical matrix using the aCLIMAX package.<sup>8</sup>

### 2.2. Density Functional Theory calculations of the vibrational density of states: $\text{Mg}^{2+}$ and $\text{Ca}^{2+}$ in solution

#### 2.2.1. Classical molecular dynamics

Classical dynamics simulations were performed using version 4.03.3 of the DL\_POLY molecular dynamics package.<sup>9</sup> The leapfrog algorithm with a time step of 5 fs was used to integrate the equations of motion. The isothermal-isobaric (constant NPT) ensemble was used to maintain a temperature of 300 K and a pressure of 1 bar. The weak-coupling algorithms of Barendsen and co-workers<sup>10</sup> were used with 0.1 ps and 1.0 ps as the thermostat and barostat relaxation times, respectively. The electrostatic forces were calculated by means of the Ewald summation method.<sup>11</sup> A value of  $0.54722 \text{ sÅ}^{-1}$  was used for the Ewald convergence parameter with a 6.0 Å cutoff for the real-space part of the Ewald sum. A value of 14 was used for the maximum  $k$ -vector index in all three directions in the reciprocal space. Together these three parameters correspond to a relative error in the Coulombic energy of  $10^{-6}$ . A 6.0 Å cutoff was also used for the van der Waals forces. The water molecules were represented using the extended simple point charge (SPC/E) potential.<sup>12</sup> In the SPC/E model, the geometry of the water molecule is fixed such that the OH distance is 1.0 Å and the HOH angle is equal to  $109.47^\circ$ . The geometry of the water molecules was held fixed by the SHAKE algorithm.<sup>13</sup> For the  $\text{Ca}^{2+}$ –water interaction and  $\text{Mg}^{2+}$ –water interactions we used the Buckingham potentials parameterized by de Leeuw.<sup>14,15</sup>

#### 2.2.2. Ab initio molecular dynamics

Ab initio (Born-Oppenheimer) molecular dynamics (AIMD) simulations were conducted with the electronic structure code CP2K/Quickstep code, version 2.7.<sup>16</sup> CP2K implements density functional theory (DFT) based on a hybrid Gaussian plane wave. We used both the PBE<sup>7</sup> and BLYP<sup>17,18</sup> generalized gradient approximation for the exchange and correlation terms together with the general dispersion correction termed DFT-D3.<sup>19</sup> Goedecker-Teter-Hutter pseudopotentials<sup>20</sup> were used to describe the core–valence interactions. All atomic species were represented using a double-zeta valence polarized basis set. The plane wave kinetic

energy cut off was set to 1000 Ry. k-sampling was restricted to the  $\Gamma$  point of the Brillouin zone. Simulations were carried out with a wave function optimization tolerance of  $10^{-6}$  au that allows for 1.0 fs time steps with reasonable energy conservation. Periodic boundary conditions were applied throughout. AIMD simulations were carried out in the NVT ensemble using a Nosé-Hoover chain thermostat to maintain the average temperature at  $T = 300\text{K}$ .

### 2.2.3. Simulation protocol

Starting from the last configuration of 200 ps of NPT simulation of 64 water molecules, one H<sub>2</sub>O molecule was replaced by one  $M^{2+}$  ( $M = \text{Mg}$  and  $\text{Ca}$ ) ion. For each hydrated ion, we conducted classical MD simulations of 1000 ps in length, followed by 40 ps of AIMD simulations. For comparison, AIMD simulations of pure bulk water were also considered.

### 2.2.3. Analysis

**Vibrational density of states.** Vibrational properties of the water molecules were computed using the ab initio MD trajectories and relied on the calculation of the velocity-autocorrelation function (VACF) of oxygen and hydrogen atoms. VACF is defined as follows:

$$VACF(t) = \frac{1}{N_o N_{atm}} \sum_{j=1}^{N_o} \sum_{i=1}^{N_{atm}} \mathbf{v}_i(t_j) \cdot \mathbf{v}_i(t_j + t) \quad (1)$$

where  $\mathbf{v}_i$  is the velocity vector of O or H atoms in the water molecule  $i$ ,  $N_o$  is the number of time origins spaced by  $t$  and  $N_{atm}$  is the number of O or H atoms. From the Fourier transform of the VACF of each atom, the vibrational density of states (VDOS) of each atom was then calculated. In order to investigate the local effect of the metal cations, the averages in eq. (1) were restricted to the water molecules belonging to the hydration shell of  $\text{Ca}^{2+}$  and  $\text{Mg}^{2+}$ . The first hydration shell of calcium and magnesium were defined using the spherical cutoff of 3.0 Å and 3.2 Å, respectively, which correspond to the position of the first minimum of the radial distribution function between the metal cation and the oxygen atom of water.

**Characterization of the dynamics of the hydration shell of ions.** The dynamics of the first hydration shell of magnesium and calcium ions in water were characterized using the “direct” method proposed by Hofer and co-workers.<sup>21</sup> This method was successfully applied for, among others, the characterization of the dynamics of the coordination shell of hydrated alkaline earth metal ions and their carbonate and bicarbonate complexes<sup>22</sup> and the quantification of the water exchange frequency at structurally distinct calcium sites on the calcite surface.<sup>23</sup> The classical MD trajectories were analysed for water molecule movements and whenever a water molecule crossed the boundary of the metal ion coordination shell its path was followed; if the new position of the water molecule outside or inside this shell lasted for more than 0.5 ps the event was accounted as a real exchange event.<sup>21</sup> The coordination shells of  $\text{Mg}^{2+}$  and  $\text{Ca}^{2+}$  was defined by a cutoff radius ( $R_{\text{cutoff}}$ ), and the number of accounted water exchange events was computed as a function of an increasing cutoff radius ( $R_{\text{cutoff}}$ ).



### 3. Classical nucleation theory: linking solid state dynamics and crystallization kinetics

According to classical nucleation theory (CNT), for a solid-state nucleation process (crystallization), the change in the free energy ( $\Delta g$ ) associated to the formation of a new bulk phase is proportional to the difference in the chemical potential ( $\Delta\mu$ ) between the initial states and the final states and to the interfacial energy of the newly created interface:

$$\Delta g = \frac{3}{4} \frac{\pi r^3}{\Omega} (\mu_i - \mu_f) + 4\pi r^2 \alpha \quad (2)$$

where  $\Omega$  is the molar volume of the new phase,  $r$  is the size of the nucleus (suppose a sphere for simplicity), and  $\alpha$  is the interfacial free energy corresponding to the interface created between the amorphous matrix and the crystalline nucleus. When the nucleation barrier is high enough compared to the thermal energy,  $K_B T$ , the metastable state of the system contains thermal fluctuations that are well described by a Boltzmann distribution. Sometimes, one of these fluctuations will reach and overcome the critical size. CNT assumes that the system reaches a steady-state and stable nuclei then appear at a rate given by:

$$J_n = A e^{-\frac{\Delta g}{K_B T}} = f^* Z C_0 e^{-\frac{\Delta g}{K_B T}} \quad (3)$$

where  $f^*$  is the rate at which a critical cluster grows,  $Z$  is the Zeldovich factor and  $C_0$  is the concentration of particles (ions) in the system. The factor  $f^*$  depends on the nucleus growth mechanisms. The Zeldovich factor is determined by the energy profile around the particle of the critical size (it is therefore proportional to  $dg_n/dr$ ). Critical clusters experience random size variations that cause some of them to re-dissolve and to fall out of the stable region.<sup>24</sup> The Zeldovich factor accounts for the probability of success where only some of these clusters will continue to grow. It is a factor that effectively decreases the nucleation rate by  $f^* C_0 \exp(-\Delta g_n/K_B T)$ . As shown by Clouet,<sup>25</sup> under the assumption that the critical cluster growth is controlled by the long-range diffusion of solute atom, the nucleus growth rate  $f^*$  can be expressed as:

$$f^* = 4\pi \frac{D x^0}{\Omega y^e} \quad (4)$$

where  $x^0$  and  $y^e$  are fractions of atoms diffusing in the metastable (initial) and stable (final) phases, respectively, and  $D$  is the diffusion coefficient of the particles feeding the crystalline nucleus (under the approximation that the diffusion of a single species is limiting the growth process). This expression links therefore the diffusivity of the species being added to the growing cluster to the nucleation rate. The diffusivity,  $D$ , in eq. (3) is the self-diffusivity of a single species within the solid. To this point, the diffusivity associated to the structural relaxation measured by coherent X-rays is the so-called ‘coherent diffusivity’ which, in addition to the self-diffusivity, includes the relative displacement of one species with respect to others (*i.e.* the ‘distinct’ term of the van Hove correlation function).<sup>26,27</sup> In the case of solid state nucleation within disordered materials, such as the case for the crystallization of amorphous carbonates, the coherent diffusivity is more representative of the physical mechanisms underlying the crystallization process. It is therefore reasonable to replace  $f^*$  in eq. (2) by the following:

$$f^{coh} = \frac{D_{coh}}{\Omega} = \frac{1}{\Omega \tau q^2} = \frac{\omega}{\Omega q^2} \quad (5)$$

Eq. (2) then becomes:

$$J_n = \frac{\omega}{\Omega q^2} Z C_0 e^{-\frac{\Delta g}{K_B T}} \quad (6)$$

This expression includes a  $q$ -dependence, implying that the rate will depend on the length-scale of the observation. This dependence is countered by the ‘hydrodynamic slowing down’, i.e. the fact that the relaxation time decreases inversely proportional to  $q^2$ .<sup>26</sup> Note that the proportionality with  $q^2$  is only true for a Brownian diffusive system. Other diffusion mechanisms are present in jammed or strained systems that show compressed exponentials in the relaxation functions, with different  $q$ -dependences (e.g.,  $D \propto q^{-1}$ ). Our results show that the nature of the relaxation dynamics in amorphous carbonates is not that of an ideal Brownian system, but it displays compressed exponents ( $\beta > 1$ ) with  $1.23 < \beta < 1.85$  (see main text). The  $q$ -dependence also shows deviations from the ideal Brownian diffusivity. This is shown in Supporting Figure S11 where the time-evolution of  $q$ -dependence of the relaxation times  $\tau$  is shown for different samples. Under these circumstances, only an order of magnitude of the ‘coherent’ diffusion constant  $D_{\text{coh}}$  is obtained assuming  $q^{-2}$  dependence from a regression of  $\tau = 1/Dq^2$ . The estimation yields a value for  $D_{\text{coh}} \sim 10^{-20}$  m<sup>2</sup>/s. This value is much higher than values reported for other amorphous and glassy systems such as covalent or metallic glasses, which exhibit relaxation times that are at least four orders of magnitude larger.<sup>28,29</sup> XPCS experiments times performed at higher scattering vector  $q$  (atomic scale) were unsuccessful due to the very short relaxation times inaccessible to detectors employed (too fast dynamics). Amorphous hydrous carbonates can therefore be considered as ‘soft systems’ as described also by the self-diffusivity of Ca<sup>2+</sup> determined by computer simulations, which is close to that of molecular species in organic solvents.<sup>30</sup>

## References

- (1) *ILL Neutron Data Booklet*, 2nd ed.; Dianoux, A. J., Lander, G., Eds.; Old City Publishing: Philadelphia, 2003.
- (2) Soler, J. M.; Artacho, E.; Gale, J. D.; García, A.; Junquera, J.; Ordejón, P.; Sánchez-Portal, D. The SIESTA Method for Ab Initio Order-N Materials Simulation. *J. Phys. Condens. Matter* **2002**, *14*, 2745.
- (3) N Troullier, J. M. Efficient Pseudopotentials for Plane-Wave Calculations. *Phys. Rev. B* **1991**, *43*, 1993.
- (4) Sánchez-Portal, D.; Junquera, J.; Paz, Ó.; Artacho, E. Numerical Atomic Orbitals for Linear-Scaling Calculations. *Phys. Rev. B - Condens. Matter Mater. Phys.* **2001**, *64*, 235111.
- (5) Anglada, E.; M. Soler, J.; Junquera, J.; Artacho, E. Systematic Generation of Finite-Range Atomic Basis Sets for Linear-Scaling Calculations. *Phys. Rev. B - Condens. Matter Mater. Phys.* **2002**, *66*, 205101.
- (6) Lee, K.; Murray, É. D.; Kong, L.; Lundqvist, B. I.; Langreth, D. C. Higher-Accuracy van Der Waals Density Functional. *Phys. Rev. B* **2010**, *82*, 081101.
- (7) Perdew, J. P., Burke, K. & Ernzerhof, M. Generalized Gradient Approximation Made Simple. *Phys. Rev. Lett.* **1996**, *77*, 3865.
- (8) Ramirez-Cuesta, A. J. ACLIMAX 4.0.1, the New Version of the Software for Analyzing and Interpreting INS Spectra. *Comput. Phys. Commun.* **2004**, *157*, 226–238.
- (9) Todorov, I. T.; Smith, W.; Trachenko, K.; Dove, M. T. DL\_POLY\_3: New Dimensions in Molecular Dynamics Simulations via Massive Parallelism. *J. Mater. Chem.* **2006**, *16*, 1911–1918.
- (10) Berendsen, H. J. C.; Postma, J. P. M.; van Gunsteren, W. F.; DiNola, A.; Haak, J. R. Molecular Dynamics with Coupling to a Heat Bath. *J. Chem. Phys.* **1984**, *81*, 3684.
- (11) Ewald, P. P. Die Berechnung Optischer Und Elektrostatischer Gitterpotentiale. *Ann. Phys.* **1921**, *369*, 253–287.
- (12) Berendsen, H. J. C.; Grigera, J. R.; Straatsma, T. P. The Missing Term in Effective Pair Potentials. *J. Phys. Chem.* **1987**, *91*, 6269–6271.
- (13) Ryckaert, J.; Ciccotti, G.; Berendsen, H. J. Numerical Integration of the Cartesian Equations of Motion of a System with Constraints: Molecular Dynamics of n-Alkanes. *J Comput Phys* **1977**, *23*, 327–341.
- (14) De Leeuw, N. H.; Parker, S. C. Atomistic Simulation of the Effect of Molecular Adsorption of Water on the Surface Structure and Energies of Calcite Surfaces. *J. Chem. Soc., Faraday Trans.* **1997**, *93*, 467–475.
- (15) Ruiz-Hernandez, S. E.; Grau-Crespo, R.; Almora-Barrios, N.; Wolthers, M.; Ruiz-Salvador, A. R.; Fernandez, N.; De Leeuw, N. H. Mg/Ca Partitioning between Aqueous Solution and Aragonite Mineral: A Molecular Dynamics Study. *Chem. - A Eur. J.* **2012**, *18*, 9828–9833.
- (16) Hutter, J.; Iannuzzi, M.; Schiffmann, F.; Vandevondede, J. Cp2k: Atomistic Simulations of Condensed Matter Systems. *Wiley Interdiscip. Rev.: Comput. Mol. Sci.* **2014**, *4*, 15–25.
- (17) Becke, A. D. Density-Functional Exchange-Energy Approximation with Correct Asymptotic Behavior. *Phys. Rev. A* **1988**, *38*, 3098.
- (18) Lee, C.; Yang, W.; Parr, R. G. Development of the Colle-Salvetti Correlation-Energy Formula into a Functional of the Electron Density. *Phys. Rev. B* **1988**, *37*, 785.
- (19) Grimme, S.; Antony, J.; Ehrlich, S.; Krieg, H. A Consistent and Accurate Ab Initio Parametrization of

- Density Functional Dispersion Correction (DFT-D) for the 94 Elements H-Pu Evaluation of DFT-D3 Dispersion Corrections for Various Structural Benchmark Sets A Consistent and Accurate Ab Initio Parametr. *J. Chem. Phys.* **2010**, *132*, 154104.
- (20) Goedecker, S.; Teter, M. Separable Dual-Space Gaussian Pseudopotentials. *Phys. Rev. B* **1996**, *54*, 1703.
  - (21) Hofer, T. S.; Tran, H. T.; Schwenk, C. F.; Rode, B. M. Characterization of Dynamics and Reactivities of Solvated Ions by Ab Initio Simulations. *J. Comput. Chem.* **2004**, *25*, 211–217.
  - (22) Di Tommaso, D.; De Leeuw, N. H. First Principles Simulations of the Structural and Dynamical Properties of Hydrated Metal Ions  $\text{Me}^{2+}$  and Solvated Metal Carbonates ( $\text{Me} = \text{Ca}, \text{Mg}, \text{and Sr}$ ). *Cryst. Growth Des.* **2010**, *10*, 4292–4302.
  - (23) Wolthers, M.; Di Tommaso, D.; Du, Z.; De Leeuw, N. H. Calcite Surface Structure and Reactivity: Molecular Dynamics Simulations and Macroscopic Surface Modelling of the Calcite-Water Interface. *Phys. Chem. Chem. Phys.* **2012**, *14*, 15145–15157.
  - (24) Kashchiev, D. *Nucleation: Basic Theory with Applications*; Butterworth-Heinemann: Oxford, 2000.
  - (25) Clouet, E. Modeling of Nucleation Processes. In *ASM Handbook Vol. 22A, Fundamentals of Modeling for Metals Processing*; Furrer, D. U., Semiatin, S. L., Eds.; ASM International: Materials Park, 2009; pp 203–219.
  - (26) Binder, K.; Kob, W. *Glassy Materials and Disordered Solids: An Introduction to Their Statistical Mechanics*, Revised.; World Scientific: Singapore, 2011.
  - (27) Ross, M.; Stana, M.; Leitner, M.; Sepiol, B. Direct Observation of Atomic Network Migration in Glass. *New J. Phys.* **2014**, *16*, 093042.
  - (28) Ruta, B.; Chushkin, Y.; Monaco, G.; Cipelletti, L.; Pineda, E.; Bruna, P.; Giordano, V. M.; Gonzalez-Silveira, M. Atomic-Scale Relaxation Dynamics and Aging in a Metallic Glass Probed by X-Ray Photon Correlation Spectroscopy. *Phys. Rev. Lett.* **2012**, *109*, 165701.
  - (29) Horbach, J.; Kob, W.; Binder, K. Dynamics of Sodium in Sodium Disilicate: Channel Relaxation and Sodium Diffusion. *Phys. Rev. Lett.* **2002**, *88*, 125502.
  - (30) Wallace, A. F.; Hedges, L. O.; Fernandez-Martinez, A.; Raiteri, P.; Gale, J. D.; Waychunas, G. A.; Whitlam, S.; Banfield, J. F.; De Yoreo, J. J. Microscopic Evidence for Liquid-Liquid Separation in Supersaturated  $\text{CaCO}_3$  Solutions. *Science* **2013**, *341*, 885–889.